High-field MRI of brain cortical substructure based on signal phase

Jeff H. Duyn†, Peter van Gelderen, Tie-Qiang Li, Jacco A. de Zwart, Alan P. Koretsky, and Masaki Fukunaga

Laboratory for Advanced MRI, Laboratory of Functional and Molecular Imaging, National Institute of Neurological Disorders and Stroke, National Institutes of Health, Building 10, Room B1D-728, 9000 Rockville Pike, Bethesda, MD 20892-1065

Edited by Leslie G. Ungerleider, National Institute of Mental Health, Bethesda, MD, and approved May 1, 2007 (received for review December 11, 2006)

The ability to detect brain anatomy and pathophysiology with MRI is limited by the contrast-to-noise ratio (CNR), which depends on the contrast mechanism used and the spatial resolution. In this work, we show that in MRI of the human brain, large improvements in contrast to noise in high-resolution images are possible by exploiting the MRI signal phase at high magnetic field strength. Using gradient-echo MRI at 7.0 tesla and a multichannel detector, a nominal voxel size of 0.24 × 0.24 × 1.0 mm³ (58 nl) was achieved. At this resolution, a strong phase contrast was observed both between as well as within gray matter (GM) and white matter (WM). In gradient-echo phase images obtained on normal volunteers at this high resolution, the CNR between GM and WM ranged from 3:1 to 20:1 over the cortex. This CNR is an almost 10-fold improvement over conventional MRI techniques that do not use image phase, and it is an ≈100-fold improvement when including the gains in resolution from high-field and multichannel detection. Within WM, phase contrast appeared to be associated with the major fiber bundles, whereas contrast within GM was suggestive of the underlying layer structure. The observed phase contrast is attributed to local variations in magnetic susceptibility, which, at least in part, appeared to originate from iron stores. The ability to detect cortical substructure from MRI phase contrast at high field is expected to greatly enhance the study of human brain anatomy *in vivo*.

anatomy | contrast mechanism | cortex

The image quality and diagnostic value of MRI of the human brain are primarily determined by the spatial resolution, signal-to-noise ratio (SNR), and tissue contrast. Because these entities are interdependent, ruled by the basic laws of NMR physics, their simultaneous improvement is not simple or straightforward. For example, reduction of the image voxel volume leads to a proportional decrease in SNR. Furthermore, excellent tissue contrast between gray matter (GM) and white matter (WM), the two main tissue components of the human brain, can be readily achieved by sensitizing the MRI acquisition technique to tissue relaxation times T_1 and T_2, but not without substantial loss in SNR. Because of these factors, clinical brain imaging on current 1.5 tesla (T) and 3.0 T scanners is limited to a resolution of ≈1 mm³ (1 μl), an SNR of 10 to 20, and an even lower contrast-to-noise ratio (CNR; see *Methods*) between GM and WM.

Recent developments in MRI technology have led to improvements in contrast and SNR. Experimental high-field scanners, operating at fields from 7.0 T to 9.4 T (1–3), allow a 2- to 3-fold improvement in image SNR over 3.0 T systems. State-of-the-art detectors based on novel multichannel technology (4–6) allow an additional 2- to 6-fold improvement in SNR depending on the brain region under study. The combined advantages of these techniques allow an order of magnitude increase in SNR or reduction of the voxel volume to <0.1 μl (7).

A major challenge of high-field MRI of the human brain is the generation of strong tissue contrast that is not affected by the technical difficulties associated with performing MRI at ≥7.0 T. For example, at high field, spatial variation in B_1 amplitude and RF power deposition in tissue increase and limit the use of efficient T_2-weighted imaging techniques such as RARE (8). T_1-weighted techniques such as magnetization-prepared rapid gradient-echo (MP-RAGE) (9) can provide excellent contrast between GM and WM, but are also hampered by B_1 power deposition issues, have relatively low SNR, and, at high resolution, require long scan times.

Several recent studies have shown that the use of MRI signal phase in gradient-echo (GRE) MRI can improve contrast MRI in specific human brain structures, including veins and iron-rich regions (10–14). Preliminary studies have also shown a substantial contrast between WM and cortical GM (11, 15). In conventional GRE, a magnitude image combines contributions from transverse (T_2) relaxation (which leads to signal decay) as well as from loss of signal because of coherence loss caused by the local resonance frequency offset or B_o shift. The latter originates, at least in part, from the magnetic susceptibility differences between tissues (10, 11). Phase imaging allows increased dynamic range in detection of these off-resonance effects by directly measuring the change in frequency offset. Phase imaging at high fields would not have some of the disadvantages of the techniques established at low field, such as the requirement for very homogeneous transmit fields that are hard to obtain at high fields or high power deposition that can occur. In addition, phase contrast is predicted to increase at higher magnetic fields.

In the current study, we explore the benefits of MRI of the brain based on susceptibility induced phase contrast at 7.0 T. First, we compare contrast based on the GRE phase with that of conventional methods such as GRE and MP-RAGE magnitude images. Subsequently, we investigate whether the use of GRE phase at high field, combined with the high spatial resolution available with multichannel detectors, allows the detection of cortical substructure in human brain.

Results

Image Quality. In all subjects, both GRE and MP-RAGE data were of excellent quality. The use of a reference scan to correct for B_1 nonuniformities proved effective because only minimal large-scale spatial variation in MP-RAGE image intensity was observed. An example is shown in Fig. 1, which compares GRE phase data with GRE magnitude data and the lower resolution MP-RAGE data. Substantial contrast in brain tissue is observed in all three types of MRI images. In addition, the GRE phase data showed substantial intensity variations near air–tissue interfaces (e.g., near the skull). These phase variations are

Author contributions: J.H.D. designed research; J.H.D., P.v.G., T.-Q.L., J.A.d.Z., A.P.K., and M.F. performed research; P.v.G., T.-Q.L., J.A.d.Z., A.P.K., and M.F. contributed new reagents/analytic tools; J.H.D., P.v.G., T.-Q.L., J.A.d.Z., A.P.K., and M.F. analyzed data; and J.H.D. wrote the paper.

The authors declare no conflict of interest.

This article is a PNAS Direct Submission.

Abbreviations: SNR, signal-to-noise ratio; CNR, contrast-to-noise ratio; GM, gray matter; WM, white matter; CSF, cerebrospinal fluid; GRE, gradient-echo; MP-RAGE, magnetization-prepared rapid gradient-echo; TR, repetition time; TE, echo time; TI, inversion time.

See Commentary on page 11513.

†To whom correspondence should be addressed. E-mail: jhd@helix.nih.gov.

www.pnas.org/cgi/doi/10.1073/pnas.0610821104

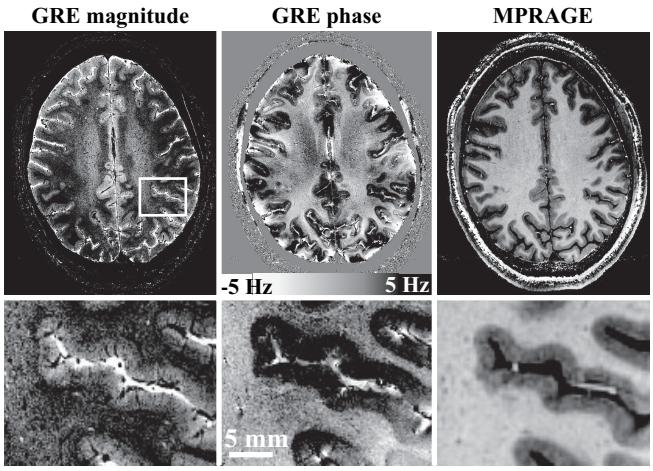

Fig. 1. Illustration of image quality of MRI based on image phase. The increased CNR available with MRI phase data allows dramatically improved resolution and shorter scan time. The GRE data (*Left* and *Center*) were acquired at a resolution of 240 × 240 μm in a scan time of 6.5 min, whereas the MP-RAGE data (*Right*) was acquired at a resolution of 480 × 480 μm in a scan time of 20 min. The scale bar in the GRE phase data shows the frequency shifts corresponding to the observed phase differences. (*Lower*) Magnifications of the area outlined in white on the GRE magnitude image (*Left Upper*). The macroscopic intensity variations in the phase image are attributed to susceptibility effects related to air–tissue interfaces.

attributed to susceptibility differences between the different tissue types caused by macroscopic phase effects that were not completely removed by the correction procedure based on polynomial fitting (see *Methods*). In addition, some phase distortions were seen in areas with very low SNR, such as the large vessels.

For both the GRE and MP-RAGE data, image SNR varied strongly over the brain. SNR was highest in peripheral cortex, a phenomenon inherent to signal reception with array detectors (16). For GRE data, SNR varied from 20:1 in the peripheral cortex to 3:1 in GM in the center of the brain. For the MP-RAGE data, WM SNR values in corresponding regions were 28:1 and 4:1, respectively.

Contrast Between GM and WM. In most brain regions, image contrast in GRE magnitude, GRE phase, and MP-RAGE data

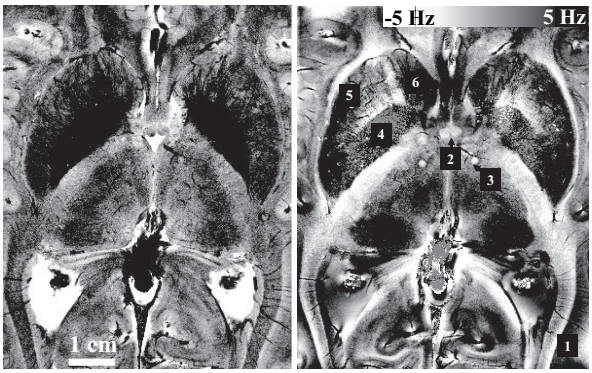

Fig. 2. Example of GRE magnitude and phase data in central brain region acquired at a 240 × 240 μm inplane resolution. Note the many anatomical details visible at this resolution, including veins crossing the optic radiations (box 1), columna fornix (box 2), cross-section of the mamillothalamic tract (box 3), globus pallidus (box 4), putamen (box 5), and head of the caudate nucleus (box 6).

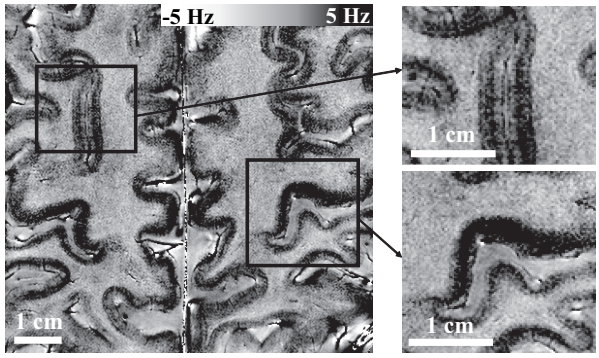

Fig. 3. Intracortical contrast in MRI signal phase. Most cortical regions show a variation intensity that is suggestive of an underlying layer structure (*Left*). The intensity pattern varies between the different gyri, with clear differences between the upper and lower banks of the central sulcus (*Right Lower*) and cortices adjacent to the superior frontal sulcus (*Right Upper*).

allowed discrimination between GM and WM regions. In the GRE magnitude data, contrast between GM and WM was variable and sometimes vanished (see Figs. 1 and 2), consistent with earlier work (7). A dramatic contrast between GM and WM was observed in the GRE phase data, indicating frequency differences of up to 6 Hz between cortical GM and underlying WM. Similar GM-WM differences were seen in all subjects. Like GRE magnitude contrast, GRE phase contrast was variable and appeared to vanish in some brain regions. In the phase data, the GM frequency was higher than that of WM and cerebrospinal fluid (CSF), corresponding to a larger (and more positive) magnetic susceptibility. Outside the major fiber bundles, little contrast was observed between WM and CSF (see Fig. 3). The GM-WM CNR of GRE phase data was generally substantially higher than of that GRE magnitude data. The improvement over

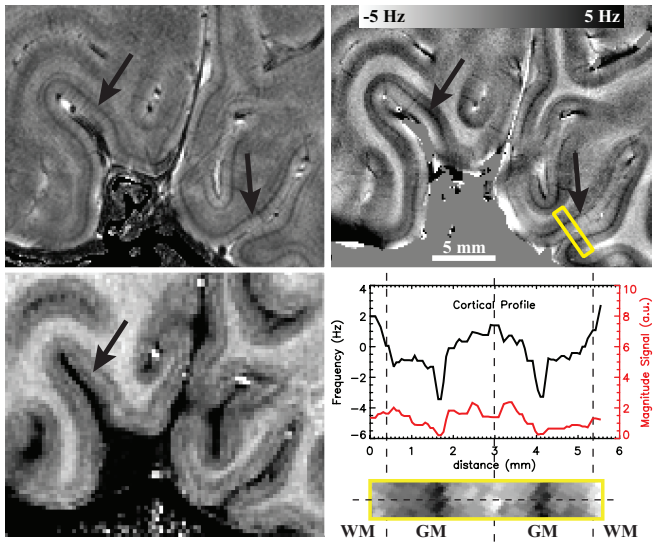

Fig. 4. Intracortical contrast in the primary visual cortex. In the GRE magnitude image (*Left Upper*) and phase image (*Right Upper*), a darkening is observed in the central layers of the cortex, resembling the stria of Gennari (black arrow). Intensity profiles along a single projection through the cortex (dotted line in zoomed area outlined by yellow box) show that this area is ≈150–250 μm wide (*Right Lower*). Note the superior CNR of the phase data compared with the magnitude data (all GRE data are displayed at identical noise levels). The observed frequency difference between central GM and WM reaches ≈6.0 Hz. Regions with central darkening in phase show a faint brightening in the MPRAGE image (*Left Lower*).

Table 1. Frequency shift, Δ*F*, between tissue types in the motor cortex (MC) area

	Δ*F* GM-CSF	Δ*F* WM-CSF	Δ*F* GM-WM
Left MC	4.44 (0.76)	−0.12 (1.04)	4.56 (0.73)
Right MC	4.31 (0.51)	−0.47 (1.22)	4.78 (1.13)
Average MC	4.38 (0.40)	−0.29 (1.01)	4.67 (0.87)

magnitude contrast can most readily be appreciated from Fig. 4, in which GRE magnitude and phase data are displayed at identical noise levels. The improvement with GRE phase data is also consistent with theory, which predicts higher CNR values by a factor of $1.8 \cdot |F_{GM} - F_{WM}|$, with F the derived tissue frequency related to the local B_o shift (see *Methods*).

As observed previously at low resolution and low field, the motor cortex region showed a relatively strong phase effect (Fig. 3) possibly because of its increased iron content (15). Table 1 summarizes the average phase shifts observed in this region, indicating an average GM-WM contrast of 4.7 ± 0.9 Hz. Because of this large frequency shift, the estimated CNR gain over magnitude data was ≈9-fold. The MP-RAGE data showed good GM-WM contrast that was relatively constant across brain regions, consistent with studies at lower field strength (Fig. 1). The uniform contrast is attributed to the adiabatic inversion pulse used for T_1-weighting, which is minimally sensitive to the substantial B_1 transmit inhomogeneities present at high field. GM-WM CNR values in central and peripheral regions for MP-RAGE were ≈1.5:1 and 8:1, respectively, compared to 3:1 and 20:1 for GRE phase data. When adjusted for the two to three times longer scan time and four times larger voxel size, the inherent CNR of MP-RAGE data was 10- to 12-fold lower than that of GRE phase data.

Contrast Within GM and WM. In contrast to the uniform intensity within tissue types in MP-RAGE images, both GRE magnitude and phase data showed a substantial heterogeneity within both GM and WM. A striking feature of the GRE scans was the dark appearance of venous vessels in both magnitude and phase data. An illustrative example is the low signal intensity caused by veins crossing the optic radiations in Fig. 2, box 1. This result is attributed to the effect of paramagnetic deoxyhemoglobin in venous blood, leading to a less negative susceptibility and a lower T_2^* (17–19) compared to surrounding tissues. The lower T_2^* forms the basis for the technique of MRI venography (20, 21). The strong effect of dark venous vessels in MRI >7.0 T has been described previously for magnitude GRE (22).

Another notable feature of GRE magnitude and phase data is the heterogeneity within WM (Figs. 1 and 2). In the magnitude data, WM contrast appeared to correlate with the location of major fiber bundles (e.g., see Fig. 2) as reported previously (7). A somewhat similar effect was present in the phase data, with a strong contrast seen between the optic radiations and the surrounding WM (Fig. 2, box 1). Also clearly standing out in the phase data were fine WM structures such as the columna fornix (box 2) and the mamillothalamic tract (box 3), and GM structures such as the globus pallidus (box 4), the putamen (box 5), and the head of the caudate (box 6). Strong phase contrast in these GM structures has been reported previously at 1.5 T and attributed to local deposits of iron (23).

Apart from the phase effects apparently associated with pial veins on the cortical surface and principal intracortical veins traversing the cortex, several other features were present within cortical GM in the phase images. Interestingly, in many cortical regions, including the motor cortex, phase variations across the cortical thickness were observed, suggesting a layer-specific contrast (Figs. 3, 4, and 5*a*). In general, contrast of GM with CSF and WM was strongest in the deeper layers of the cortex. A notable exception was the primary visual cortex (Fig. 4), where contrast was most prominent in the central layers. The dark banding in the GRE phase data corresponded to a darkening in the GRE magnitude data and a faint brightening in the MP-RAGE data. The latter has been observed previously and is attributed to the stria of Gennari (24, 25), a myelin-rich region in the primary visual cortex.

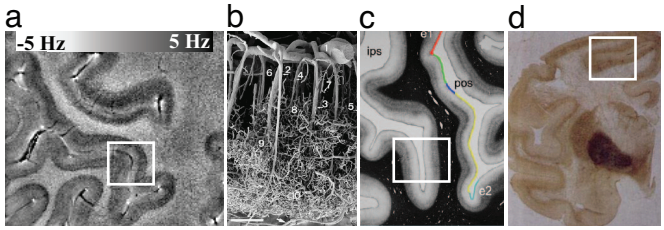

Fig. 5. Illustration of possible origins of MRI phase contrast. (*Insets*) Cortical areas with layer-specific contrast. The increasing contrast seen in the deeper layers of the cortex (*a*, our data) is consistent with multiple hypothesized origins, including vascular density/hemoglobin content (*b*; corrosion cast of cortical vasculature reproduced from ref. 38), myelin concentration (*c*; myelin silver stain reproduced from ref. 39), and iron concentration (*d*; Perl's iron stain reproduced from ref. 44).

Discussion

General Remarks. The results presented here indicate that high-field MRI combined with multichannel detection and phase-based contrast allows *in vivo* brain imaging with unprecedented CNR and resolution. Excellent image quality was obtained at 58-nl voxel resolution, owing in part to the suppression of ghosting artifacts through real-time shimming of the B_o field (26). At this high resolution, a substantial phase contrast is seen both between as well as within GM and WM. In the cerebral cortex, a contrast pattern suggestive of an underlying layer structure was observed. MRI phase contrast in GRE images has been attributed to magnetic susceptibility differences, which can originate from a variety of sources, including tissue iron and myelin content and deoxygenated hemoglobin in blood (for further discussion, see *Origin of Phase Contrast*).

The large degree of signal heterogeneity reported here in both GM and WM using phase imaging originates from and allows detection of the underlying anatomy. There have been a few papers that have detected a small number of specific areas of WM heterogeneity using conventional MRI contrast at lower fields (27–29). However, none of these papers reported the widespread heterogeneity detected in the present work. Recently, we reported extensive heterogeneity throughout WM using magnitude GRE at 7.0 T (7). These results are replicated here, and the contrast was improved by using signal phase. It is clear that the contrast relates to specific fiber bundles, as well as tissue heterogeneity within regions of WM. Similarly, there have been a few reports of GM heterogeneity detected with T_1-based MRI of the human brain (30, 31). The phase imaging reported here reveals large changes in contrast as one goes around the cortex, most notably through the motor cortex. Recently, a number of groups have reported contrast across the cortex that has been attributed to myelin differences in the different cortical layers (24, 25, 32–34). The primarily T_1-based contrast used in these studies is much lower than that found between GM and WM, making it difficult to routinely detect cortical substructure. In the present work, substantial heterogeneity was detected in the phase images obtained at 7.0 T across the cortex. Because phase imaging allowed a much larger CNR than that available with T_1-based contrast, it should prove useful as a robust approach for noninvasively studying cytoarchitecture of individ-

ual brains. Indeed the ability to clearly detect cortical lamination in the visual cortex and a striking transition into the motor cortex suggests that phase imaging at 7.0 T will enable identification of a number of brain areas.

CNR. The GRE phase data suggested substantial frequency differences between cortical GM and nearby WM, which in some brain regions reached ≈6 Hz. Because of these large frequency differences, the CNR of the GRE phase data between these tissues was far superior to that of the GRE magnitude and MP-RAGE data. Theoretical considerations indicate that almost an order of magnitude increase in CNR can be obtained when using GRE phase data, rather than the conventionally used magnitude data (see *Methods*). The CNR of GRE phase data were also far superior to (10–12 times) the CNR available with MP-RAGE, a technique conventionally used to generate GM–WM contrast.

Contrast Uniformity. Although CNR of the GRE phase data was generally far superior to that of MP-RAGE, a number of factors caused it to vary strongly across brain regions. In addition to coil sensitivity variations, important contributors are the tissue's chemical composition and geometry. The latter comes into play through the inherent geometric properties of magnetic susceptibility effects. As a result, phase effects are generally not constrained to the area of altered susceptibility, but might affect the surrounding area. However, in principle, it is possible to reconstruct the tissue susceptibility distribution from the acquired phase data, provided that 3D data are available covering a large volume (15, 35). This reconstruction was not attempted in the current study because 3D high-resolution GRE acquisition required prohibitively long scan times with the current technology. The use of image acceleration with parallel imaging should alleviate this problem (36, 37).

Origin of Phase Contrast. Although speculations have been made about the origins of the tissue susceptibility differences underlying MRI phase contrast, firm establishment of the underlying contrast mechanism has been hampered by the lack of quantitative data. The data obtained in the current study invite an updated review of the potential contribution of some of the major sources of susceptibility contrast.

Deoxy-Hemoglobin. Deoxygenated red blood cells are paramagnetic and could induce substantial phase shifts in GRE data. In fact, the GRE magnitude and phase data showed clear evidence of vascular structures in both GM and WM regions. The relatively high blood volume of GM relative to WM and CSF could explain some of the phase differences seen between these tissue types. In addition, contrast within GM might be caused by the variations in vascular density and blood oxygenation. In fact, vascular density has been reported to vary both across the cortex and with cortical depth (38), with a higher density often observed in the deeper layers (Fig. 5*b*). This is consistent with the varying cortical phase contrast, with increased phase effects often seen in the deeper layers (Fig. 5*a*). However, simple calculation shows that deoxy-hemoglobin effects can, at best, only partly explain the magnitude of the observed phase differences. Assuming a susceptibility difference of 1.15 ppm between pure water and fully deoxygenated red blood with 45% hematocrit (17–19), an average blood deoxygenation fraction of 30%, and a cortical blood volume of 4%, the estimated susceptibility difference $\Delta\chi$ between GM and CSF is +0.02 ppm. In this estimate, it is assumed that CSF has a susceptibility similar to that of pure water (−9.05 ppm at 37°C). At 7 T (F_0 = 298 MHz), a susceptibility shift $\Delta\chi$ results in a nuclear frequency shift ΔF of up to $\frac{1}{3} \cdot F_0 \cdot \Delta\chi$ (15, 35), which corresponds to ≈2 Hz. This seems too low to explain the frequency shifts of ≈6 Hz observed in the current study. In addition, because most deoxygenated blood is situated in the pial vasculature, one would expect deoxy-hemoglobin effects to be most apparent on the cortical surface. This was not the case because typically stronger phase shifts were observed deeper in the cortex.

Myelin. The concentration of myelin is higher in WM than in GM and also varies across cortical layers. For example, a silver stain specific to myelin is reproduced in Fig. 5*c* (39), showing increased myelin content in the deeper cortical layers with a pattern similar to that observed in the MRI phase data. Some of the observed phase effects might be because of lipids, which are relatively abundant in myelin. The total lipid fraction is ≈7% in GM, ≈16% in WM (40), and ≈0% in CSF. Although the magnetic properties of lipids are different from those of water, $\Delta\chi$ values are strongly dependent on the type of lipid. The lipids with the largest differences in abundance between GM and WM are cholesterol and cerebroside (40). Assuming cholesterol-like magnetic properties for all brain lipids, $\chi_{\text{cholesterol}} = -9.23$ ppm (41), we find $\Delta\chi = -0.18$ ppm relative to CSF (−9.05 ppm), corresponding to $\Delta F = -1.4$ Hz and −3.0 Hz for GM and WM, respectively. These shifts are inconsistent with the experimental findings, which indicate largely positive shifts in GM and small negative shifts in WM (e.g., +4.38 and −0.29 Hz, respectively, in the motor cortex area; see Table 1). In addition, a myelin-based origin would result in a similar frequency shift in WM and the myelin-rich stripe of Gennari in V1, which is contrary to the large (≈6 Hz) differences (slightly negative vs. strongly positive, respectively) found in practice (see Fig. 4).

Iron. Several reports have implicated nonheme iron as the source of MRI phase contrast (15, 23, 42), specifically, in some of the iron-rich brain nuclei, such as the substantia nigra and red nucleus. In the cortex, regional variations in T_2 have been attributed to cortical variation in iron concentration, rather than to blood volume differences (43). Perl's iron stains of brain sections from a rhesus monkey (44) and humans (45, 46) indicate a GM iron concentration that varies across cortical layers, with deeper layers having the highest iron concentration. Similarity with the MRI phase data are illustrated in Fig. 5*d*, which is a reproduction of the Perl's iron stain from ref. 44. Most human brain iron is found within the iron storage protein ferritin and its breakdown product, hemosiderin (47). Assuming minimal saturation of the ferritin iron core, $\Delta\chi$ due to tissue iron is ≈1.4 ppm for each milligram of iron per gram of tissue (19). In cortical GM, histological ferritin concentrations are quite variable, ≈0.04 mg/g (48, 49), whereas CSF levels are ≈0.003 mg/g (50). These values lead to $\Delta\chi = 0.05$ ppm, equivalent to $\Delta F = 5.0$ Hz. This is consistent with the frequency shift observed between GM and CSF. An iron-based contrast mechanism also would suggest that the central layers of the visual cortex, which show a strong phase contrast (Fig. 4), might have an increased iron concentration. Iron content is an alternative or additional explanation for the earlier observed T_1 contrast in this region, which has been attributed to myelin (24).

However, histological studies also show that WM iron concentrations are similar to those in GM (48, 49), which does not explain the strong phase differences seen between GM and WM. In addition, a low iron concentration in the optic radiations could explain their bright appearance in GRE phase images (Fig. 2), but by itself does not explain their dark appearance in the GRE magnitude data. Although iron is likely to have some contribution to the observed phase contrast, it does not fully explain the current findings. Clearly more research needs to be done to establish the relative contributions of each of the proposed contrast mechanisms. Ideally, this research should include studies of *in vivo* MRI phase and postmortem iron and myelin stains and histochemistry on the same tissue.

Potential of High-Resolution MRI Based on Tissue Susceptibility. The data presented in the current study suggests that imaging of laminar structure within the cortex is possible when exploiting susceptibility contrast and the increased SNR available with high-field MRI systems and multichannel detection. Combined, these methods enable an almost 100-fold improvement in GM-WM CNR over conventional methodology (i.e., MP-RAGE techniques performed at low field) and single-channel signal detection. This CNR gain is essential to achieve the resolution required to image laminar structure within the cortex. Indeed, with this high CNR, it should be possible to sacrifice some CNR and obtain even higher resolution images. However, motion-correction algorithms might be required to go much beyond the 240 μm in plane resolution used in the present study (51, 52).

Other than firmly establishing its origin, more work needs to be done before the demonstrated phase contrast can be fully exploited. Better correction algorithms need to be developed to correct for the macroscopic phase effects from susceptibility gradients surrounding the brain, such as the tissue–skull and skull–air interfaces. In addition, rapid scan techniques will need to be developed to collect data over the entire brain, which is required for proper calculation of susceptibility distributions from phase data. This calculation will be facilitated by 3D MRI acquisition of isotropic voxels (rather than the strongly anisotropic voxels currently acquired), and modeling of brain–skull boundaries. Last, additional improvement of the spatial resolution is expected from the development of MRI at even higher magnetic field strength and employing detectors with a higher number of coil elements. This improvement should lead to a further reduction in voxel volumes.

Although the origin of the observed intracortical susceptibility contrast is unknown, there are several candidates that have potential significance for practical applications. Mapping of myelin content in both GM and WM might be important for the study of diseases such as multiple sclerosis and amyotrophic lateral sclerosis. Focal accumulations of iron have been implicated in various pathologies, including Alzheimer's disease (53–55) and multiple sclerosis (56). Phase contrast-based blood volume maps might be important for the study of vascular dementia and subtle brain infarcts. Last, intracortical phase contrast might be reflective of the tissue's underlying structure and possibly function and complement information obtained with *ex vivo* methods that map cytoarchitecture (57), myeloarchitecture (58), and receptor architecture (59). This information could be extracted through analysis of laminar profiles similar to existing methods based on histology (60) and T_1- (34) or proton density-weighted MRI (61).

Methods

MRI Data Acquisition. MRI experiments were performed on a 7.0 T GE Signa MRI scanner (GE Medical Systems, Milwaukee, WI) operated with a 24- (Figs. 1, 2, 3, and 5) or 32-channel (Fig. 4) receive-only detector array (Nova Medical, Wilmington, MA) (6). Because the MRI system had a limited number (16) of receiver channels, only signals from the 16 coils closest to the brain region under study were acquired.

Seven normal volunteers (three male) ages 25–52 years were scanned under a human subject protocol approved by the Institutional Review Board of the National Institute of Neurological Disorders and Stroke/National Institutes of Health. To restrict head motion, foam pads were inserted into the space between the subject's head and the interior lining of the MRI detector array. Axial GRE acquisitions were performed with echo time (TE) = 28–31 msec, repetition time (TR) = 500 to 1,000 msec, flip angle 30 to 50° (adjusted at center of brain), slice thickness = 1 mm, field of view = 240 × 180 mm, matrix size 1,024 × 768, bandwidth 32 kHz, and first-order flow compensation on all imaging gradients. The total scan time ranged from 6.5 to 13 min. Multiple slices were acquired throughout the brain with varying interslice gaps. Before the anatomical scans, higher (up to second) order B_0 shims were adjusted to minimize macroscopic susceptibility effects. In addition, during each scan, real-time higher order shimming was performed to compensate for field fluctuations related to the respiratory cycle (26). For optimal combination of the coil signals, reference maps were acquired by using a low-resolution (128 × 96) GRE reference scan at slice locations matching those of the high-resolution acquisition, and with TE = 6 msec. This reference scan was also used to correct for image intensity variations related to nonuniformities in B_1 reception profiles and part of the intensity variations caused by flip angle variations related to nonuniformities in B_1 excitation profiles (62).

For comparison, MP-RAGE scans of GM/WM anatomy were performed with the following parameters: TE = 5.4 msec, phase-encode, TR = 11.3 msec, flip angle = 14°, slice thickness = 1 mm, field of view = 240 × 180 mm, matrix size = 512 × 384, bandwidth = 62.5 kHz, inversion time (TI) = 1.2 sec, overall TR = 3 sec, and scan time = 21 min. The standard, manufacturer-supplied adiabatic inversion pulse was used for T_1-weighting. Reference data for MP-RAGE image reconstruction were acquired at low resolution (128 × 96) by omitting the inversion pulse (62).

The reference scans for MP-RAGE and GRE did not allow for correction of contrast variations because of the nonuniform T_1-weighting introduced by inhomogeneity in the B_1 excitation profile. These contrast variations were expected to be minor, particularly for the MP-RAGE data (because of the adiabatic inversion) and the GRE phase data (because of its minimal T_1-dependence).

Image Reconstruction. Images were reconstructed by using phase-sensitive combination of the individual coil data (63) using the separately acquired coil sensitivity reference data. These reference data were spatially low-pass-filtered to an in-plane resolution of ≈1.5 cm. Coil signal combination resulted in complex-valued pixel intensities $S(x,y) = R(x,y) + i \cdot I(x,y)$, with R and I representing the real and imaginary components, respectively. Both magnitude (M) and phase images (P) were generated according to: $M(x,y) = R(x,y)^2 + I(x,y)^2$ and $P(x,y) = \arctan(I(x,y)/R(x,y))$. Phase images (obtained only for GRE data) were corrected for remaining macroscopic susceptibility effects (not compensated for by the magnetic field shimming procedure) by estimating their magnitude and distribution from a polynomial fit to the data. Eighth-order 2D polynomial functions were used on a slice-by-slice basis, taking into account any 2π phase jumps present in the data. The latter was done by first taking the spatial derivative of the phase data. The fitted macroscopic phase was then subtracted from the original phase data.

Calculation of CNR for GRE Phase and Magnitude Data. The CNR between GM and WM in GRE images can be readily calculated based on measured T_2^* values. We defined CNR as the ratio between contrast (i.e., signal difference) and thermal noise, which includes sample and instrument noise. Assuming uniform spin density and T_1-weighting, we find for magnitude data:

$$\mathrm{CNR}_{\mathrm{mag}} = \mathrm{SNR}_{\mathrm{TE}=0} \cdot \left| e^{-\mathrm{TE}/T^*_{2,\mathrm{GM}}} - e^{-\mathrm{TE}/T^*_{2,\mathrm{WM}}} \right|. \quad [1]$$

Optimum contrast is achieved at:

$$\mathrm{TE}_{\mathrm{opt}} = \ln(T^*_{2,\mathrm{GM}}/T^*_{2,\mathrm{WM}}) \cdot \frac{T^*_{2,\mathrm{WM}} \cdot T^*_{2,\mathrm{GM}}}{T^*_{2,\mathrm{WM}} - T^*_{2,\mathrm{GM}}}. \quad [2]$$

Under the condition $|T^*_{2,\mathrm{GM}} - T^*_{2,\mathrm{WM}}| \ll T^*_{2,\mathrm{GM}}$, this results in:

$$\mathrm{TE}_{\mathrm{opt}} = (T^*_{2,\mathrm{WM}} + T^*_{2,\mathrm{GM}})/2 = T^*_{2,\mathrm{av}}, \quad [3]$$

and

$$\mathrm{CNR}_{\mathrm{mag,opt}} \sim \mathrm{SNR}_{\mathrm{TE}=0} \cdot \frac{|T^*_{2,\mathrm{GM}} - T^*_{2,\mathrm{WM}}|}{e \cdot T^*_{2,\mathrm{av}}}. \quad [4]$$

For phase contrast, image noise level depends on magnitude SNR level and therefore on TE and T^*_2. Assuming $T^*_{2,\mathrm{GM}} \approx T^*_{2,\mathrm{WM}}$, we have:

$$\mathrm{CNR}_{\mathrm{phase}} = \mathrm{SNR}_{\mathrm{TE}=0} \cdot e^{-\mathrm{TE}/T^*_{2,\mathrm{av}}} \cdot 2\pi \cdot \mathrm{TE} \cdot |F_{\mathrm{GM}} - F_{\mathrm{WM}}|, \quad [5]$$

with $F_{GM} - F_{WM}$ indicating the local frequency difference between GM and WM related to differences in tissue susceptibility. Optimum contrast again is achieved at $TE_{opt} = T^*_{2,\mathrm{av}}$ leading to:

$$\mathrm{CNR}_{\mathrm{phase,opt}} = \mathrm{SNR}_{\mathrm{TE}=0} \cdot 2\pi \cdot T^*_{2,\mathrm{av}} \cdot |F_{\mathrm{GM}} - F_{\mathrm{WM}}|/e. \quad [6]$$

Comparing Eqs. **4** and **6** we find:

$$\frac{\mathrm{CNR}_{\mathrm{phase,opt}}}{\mathrm{CNR}_{\mathrm{mag,opt}}} = 2\pi \cdot (T^*_{2,\mathrm{av}})^2 \frac{|F_{\mathrm{GM}} - F_{\mathrm{WM}}|}{|T^*_{2,\mathrm{GM}} - T^*_{2,\mathrm{WM}}|}.$$

For $T^*_{2,\mathrm{GM}} = 36$ msec, and $T^*_{2,\mathrm{WM}} = 32$ msec at 7.0 T (7), this leads to:

$$\frac{\mathrm{CNR}_{\mathrm{phase}}}{\mathrm{CNR}_{\mathrm{mag}}} = 1.8 \cdot |F_{\mathrm{GM}} - F_{\mathrm{WM}}|.$$

We thank Susan O'Flahavan for her assistance with the experiments, Alberto Bizzi for helpful discussions, and Karin Shmueli for her editing of the manuscript.

1. Vaughan JT, Garwood M, Collins CM, Liu W, DelaBarre L, Adriany G, Andersen P, Merkle H, Goebel R, Smith MB, Ugurbil K (2001) *Magn Reson Med* 46:24–30.
2. Robitaille PM, Warner R, Jagadeesh J, Abduljalil AM, Kangarlu A, Burgess RE, Yu Y, Yang L, Zhu H, Jiang Z, *et al*. (1999) *J Comput Assist Tomogr* 23:808–820.
3. Vaughan T, Delabarre L, Snyder C, Tian J, Akgun C, Shrivastava D, Liu W, Olson C, Adriany G, Strupp J, *et al*. (2006) *Magn Reson Med* 56:1274–1282.
4. de Zwart JA, Ledden PJ, van Gelderen P, Bodurka J, Chu R, Duyn JH (2004) *Magn Reson Med* 51:22–26.
5. Wiggins GC, Triantafyllou C, Potthast A, Reykowski A, Nittka M, Wald LL (2006) *Magn Reson Med* 56:216–223.
6. Ledden PJ, Mareyam A, van Gelderen P, Wang S, Duyn JH (2006) *Proc Ann Mtg Intl Soc Magn Res Med*, p 422.
7. Li TQ, van Gelderen P, Merkle H, Talagala L, Koretsky AP, Duyn J (2006) *NeuroImage* 32:1032–1040.
8. Hennig J, Nauerth A, Friedburg H (1986) *Magn Reson Med* 3:823–833.
9. Mugler JP, III, Brookeman JR (1990) *Magn Reson Med* 15:152–157.
10. Haacke EM, Xu Y, Cheng YC, Reichenbach JR (2004) *Magn Reson Med* 52:612–618.
11. Abduljalil AM, Schmalbrock P, Novak V, Chakeres DW (2003) *J Magn Reson Imag* 18:284–290.
12. Yamada N, Imakita S, Sakuma T, Takamiya M (1996) *Radiology* 198:171–178.
13. Rauscher A, Sedlacik J, Barth M, Mentzel HJ, Reichenbach JR (2005) *Am J Neuroradiol* 26:736–742.
14. Wycliffe ND, Choe J, Holshouser B, Oyoyo UE, Haacke EM, Kido DK (2004) *J Magn Reson Imag* 20:372–377.
15. Haacke EM, Cheng NY, House MJ, Liu Q, Neelavalli J, Ogg RJ, Khan A, Ayaz M, Kirsch W, Obenaus A (2005) *Magn Reson Imag* 23:1–25.
16. Roemer PB, Edelstein WA, Hayes CE, Souza SP, Mueller OM (1990) *Magn Reson Med* 16:192–225.
17. Ogawa S, Lee TM (1990) *Magn Reson Med* 16:9–18.
18. Thulborn KR, Waterton JC, Matthews PM, Radda GK (1982) *Biochim Biophys Acta* 714:265–270.
19. Schenck JF (1992) *Ann NY Acad Sci* 649:285–301.
20. Reichenbach JR, Haacke EM (2001) *NMR Biomed* 14:453–467.
21. Reichenbach JR, Essig M, Haacke EM, Lee BC, Przetak C, Kaiser WA, Schad LR (1998) *Magma* 6:62–69.
22. Christoforidis GA, Bourekas EC, Baujan M, Abduljalil AM, Kangarlu A, Spigos DG, Chakeres DW, Robitaille PM (1999) *J Comput Assist Tomogr* 23:857–866.
23. Ogg RJ, Langston JW, Haacke EM, Steen RG, Taylor JS (1999) *Magn Reson Imag* 17:1141–1148.
24. Clark VP, Courchesne E, Grafe M (1992) *Cereb Cortex* 2:417–424.
25. Barbier EL, Marrett S, Danek A, Vortmeyer A, van Gelderen P, Duyn J, Bandettini P, Grafman J, Koretsky AP (2002) *Magn Reson Med* 48:735–738.
26. van Gelderen P, de Zwart JA, Starewicz P, Hinks RS, Duyn JH (2007) *Magn Reson Med* 57:362–368.
27. Curnes JT, Burger PC, Djang WT, Boyko OB (1988) *Am J Neuroradiol* 9:1061–1068.
28. Kitajima M, Korogi Y, Takahashi M, Eto K (1996) *Am J Neuroradiol* 17:1379–1383.
29. Hajnal JV, De Coene B, Lewis PD, Baudouin CJ, Cowan FM, Pennock JM, Young IR, Bydder GM (1992) *J Comput Assist Tomogr* 16:506–513.
30. Steen RG, Reddick WE, Ogg RJ (2000) *Magn Reson Imag* 18:361–368.
31. Fischl B, Salat DH, van der Kouwe AJ, Makris N, Segonne F, Quinn BT, Dale AM (2004) *NeuroImage* 23(Suppl 1):S69–S84.
32. Eickhoff S, Walters NB, Schleicher A, Kril J, Egan GF, Zilles K, Watson JD, Amunts K (2005) *Hum Brain Mapp* 24:206–215.
33. Bridge H, Clare S, Jenkinson M, Jezzard P, Parker AJ, Matthews PM (2005) *J Vis* 5:93–102.
34. Walters NB, Egan GF, Kril JJ, Kean M, Waley P, Jenkinson M, Watson JD (2003) *Proc Natl Acad Sci USA* 100:2981–2986.
35. Salomir R, de Senneville BD, Moonen CTW (2003) *Conc Magn Reson B* 19B:26–34.
36. Sodickson DK, Manning WJ (1997) *Magn Reson Med* 38:591–603.
37. Pruessmann KP, Weiger M, Scheidegger MB, Boesiger P (1999) *Magn Reson Med* 42:952–962.
38. Reina-De La Torre F, Rodriguez-Baeza A, Sahuquillo-Barris J (1998) *Anat Rec* 251:87–96.
39. Annese J, Pitiot A, Dinov ID, Toga AW (2004) *NeuroImage* 21:15–26.
40. O'Brien JS, Sampson EL (1965) *J Lipid Res* 6:537–544.
41. Weast RC, Astle MC (1981–1982) *CRC Handbook of Chemistry and Physics* (Chemical Rubber, Boca Raton, FL).
42. Schenck JF, Zimmerman EA (2004) *NMR Biomed* 17:433–445.
43. Zhou J, Golay X, van Zijl PC, Silvennoinen MJ, Kauppinen R, Pekar J, Kraut M (2001) *Magn Reson Med* 46:401–406.
44. Bizzi A, Brooks RA, Brunetti A, Hill JM, Alger JR, Miletich RS, Francavilla TL, Di Chiro G (1990) *Radiology* 177:59–65.
45. Drayer B, Burger P, Darwin R, Riederer S, Herfkens R, Johnson GA (1986) *Am J Roentgenol* 147:103–110.
46. Morris CM, Candy JM, Oakley AE, Bloxham CA, Edwardson JA (1992) *Acta Anat (Basel)* 144:235–257.
47. Schenck JF (2003) *J Neurol Sci* 207:99–102.
48. Hallgren B, Sourander P (1958) *J Neurochem* 3:41–51.
49. Hallgren B, Sourander P (1960) *J Neurochem* 5:307–310.
50. Clardy SL, Earley CJ, Allen RP, Beard JL, Connor JR (2006) *J Lab Clin Med* 147:67–73.
51. Speck O, Hennig J, Zaitsev M (2006) *Magma* 19:55–61.
52. Ward HA, Riederer SJ, Grimm RC, Ehman RL, Felmlee JP, Jack CR, Jr (2000) *Magn Reson Med* 43:459–469.
53. Benveniste H, Einstein G, Kim KR, Hulette C, Johnson GA (1999) *Proc Natl Acad Sci USA* 96:14079–14084.
54. Jack CR, Jr, Wengenack TM, Reyes DA, Garwood M, Curran GL, Borowski BJ, Lin J, Preboske GM, Holasek SS, Adriany G, Poduslo JF (2005) *J Neurosci* 25:10041–10048.
55. Zhang J, Yarowsky P, Gordon MN, Di Carlo G, Munireddy S, van Zijl PC, Mori S (2004) *Magn Reson Med* 51:452–457.
56. Craelius W, Migdal MW, Luessenhop CP, Sugar A, Mihalakis I (1982) *Arch Pathol Lab Med* 106:397–399.
57. Brodmann K (1909) *Vergleichende Lokalisationlehre der Grosshirnrinde* (Barth-Verlag, Leipzig).
58. Vogt O (1911) *J Psychol Neurol* 18:107–118.
59. Geyer S, Ledberg A, Schleicher A, Kinomura S, Schormann T, Burgel U, Klingberg T, Larsson J, Zilles K, Roland PE (1996) *Nature* 382:805–807.
60. Schleicher A, Amunts K, Geyer S, Kowalski T, Schormann T, Palomero-Gallagher N, Zilles K (2000) *J Chem Neuroanat* 20:31–47.
61. Augustinack JC, van der Kouwe AJ, Blackwell ML, Salat DH, Wiggins CJ, Frosch MP, Wiggins GC, Potthast A, Wald LL, Fischl BR (2005) *Ann Neurol* 57:489–494.
62. van Gelderen P, Koretsky AP, de Zwart JA, Duyn JH (2006) *Proc Ann Mtg Intl Soc Magn Res Med*, p 2355.
63. de Zwart JA, Ledden PJ, Kellman P, van Gelderen P, Duyn JH (2002) *Magn Reson Med* 47:1218–1227.